

# Ocular Biometrics by Score-Level Fusion of Disparate Experts

Hugo Proença, *Senior Member, IEEE*

**Abstract**—The concept of periocular biometrics emerged to improve the robustness of iris recognition to degraded data. Being a relatively recent topic, most of the periocular recognition algorithms work in a holistic way, and apply a feature encoding / matching strategy without considering each biological component in the periocular area. This not only augments the correlation between the components in the resulting biometric signature, but also increases the sensitivity to particular data covariates. The main novelty in this paper is to propose a periocular recognition ensemble made of two disparate components: 1) one expert analyses the iris texture and exhaustively exploits the multi-spectral information in visible-light data; 2) another expert parameterises the shape of eyelids and defines a surrounding dimensionless region-of-interest, from where statistics of the eyelids, eyelashes and skin wrinkles / furrows are encoded. Both experts work on disjoint regions of the periocular area and meet three important properties: 1) they produce practically independent responses, which is behind the better performance of the ensemble when compared to the best individual recogniser; 2) they don't share particularly sensitivity to any image covariate, which accounts for augmenting the robustness against degraded data. Finally, it should be stressed that we disregard information in the periocular region that can be easily forged (e.g., shape of eyebrows), which constitutes an active anti-counterfeit measure. An empirical evaluation was conducted on two public data sets (FRGC and UBIRIS.v2), and points for consistent improvements in performance of the proposed ensemble over the state-of-the-art periocular recognition algorithms.

**Index Terms**—Biometrics, iris recognition, periocular recognition, visual surveillance.

## I. INTRODUCTION

Several attempts have been made to bridge the gap between *biometrics* and *visual surveillance*, seeking for computational agents that perform recognition *in-the-wild*, i.e., from large distances, under uncontrolled lighting environments and without requiring any human participation in the process. A particular branch of research uses visible-light iris data for such purpose, which is difficult due to the artefacts that degrade the resulting images.

As an attempt to increase the robustness of iris recognition in visible-light data, the concept of *periocular* biometrics has emerged, which compensates for the degradation in iris data by considering the discriminating information in the surroundings of the eye (eyelids, eyelashes, eyebrows and skin texture). Currently, the most relevant algorithms work in a holistic way:

they define a region-of-interest (ROI) around the eye and use a feature encoding / matching algorithm regardless of the biological component in each point of the ROI. However, this augments the probability of sensitivity to some data covariate and the correlation between the scores extracted from the different points in the ROI.

This paper proposes a non-holistic approach to periocular recognition. Under an atomistic criterium, we devised two experts that use disjoint data, radically different recognition strategies and attain very different effectiveness. Here, we employ the term *weak* to refer to a recognition system that yields a poor separable decision environment, i.e., where the distributions of the genuine / impostor pairwise scores largely overlap. In opposition, the term *strong* refers to a system where the distributions of genuine and impostor scores almost don't overlap, resulting in a clearly separable decision environment and low error rates.

In our ensemble, the strong expert analyses the multi-spectral information in the iris texture, according to an automatically optimised set of multi-lobe differential filters (MLDF). Complementary, the weak expert parameterises the boundary of the visible cornea and defines a dimensionless ROI that comprises the eyelids, eyelashes and the surrounding skin. This expert helps to discriminate between individuals and has three interesting properties: 1) it analyses data that has an appearance independent of the iris texture; 2) it shows reduced sensitivity to the most problematic iris image covariates; and 3) it exclusively analyses traits that cannot be easily forged by anyone not willing to be recognised, which is in opposition to the traits classically used in periocular recognition (e.g., the shape of eyebrows). We encode the shape of eyelids, the distribution and shape of the eyelashes and the morphology of the skin wrinkles / furrows in the eyelids, which are determined by the movements of the *orbicularis oculi* muscles family. Fig. 1 overviews the proposed recognition ensemble and highlights some of its disruptive features with respect to the existing works.

It is evident that using multiple sources for biometric recognition is not a new idea, and some controversy remains: is it actually an effective way to improve performance? It is argued that when a stronger and a weaker expert are combined, the resulting decision environment is averaged and the performance will be somewhere between that of the two experts considered individually [7]. Due to the way our ensemble was designed, our experiments support a radically different conclusion: even when the fused responses come from experts with very distant performance, the ensemble attains much better performance than the stronger expert (iris). This

Copyright © 2013 IEEE. Personal use of this material is permitted. However, permission to use this material for any other purposes must be obtained from the IEEE by sending a request to [pubs-permissions@ieee.org](mailto:pubs-permissions@ieee.org). Author is with the Department of Computer Science, IT - Instituto de Telecomunicações, University of Beira Interior, 6200-Covilhã, Portugal. [hugomcp@di.ubi.pt](mailto:hugomcp@di.ubi.pt)

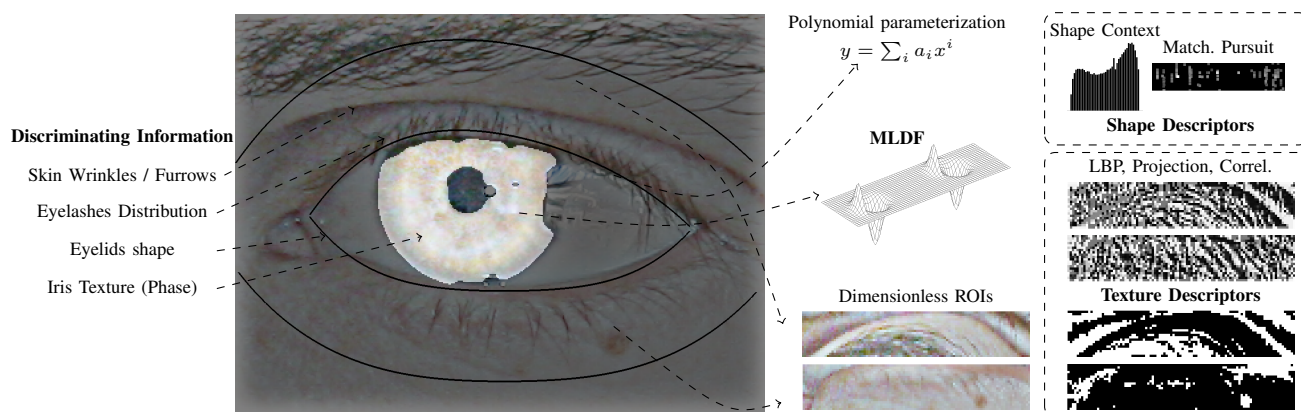


Fig. 1. Cohesive overview of the ensemble recognition method proposed in this paper: a *strong* biometric expert encodes the information inside the iris by multi-lobe differential filters. The *weak* expert is based in the polynomial parameterisation of the shape of the visible cornea, from where two dimensionless regions-of-interest are defined. Shape and texture descriptors encode the discriminating information.

is due to the fact that both experts produce quasi-independent responses and are not particularly sensitive to the same image covariate, augmenting the robustness against degraded data.

The remainder of this paper is organised as follows: Section II contextualises the problem and summarises the most relevant algorithms published. Sections III and IV describe the strong and weak biometric experts. In section V we report the empirical evaluation and compare our algorithm to the state-of-the-art. Finally, section VI concludes this paper.

## II. OCULAR RECOGNITION ON DEGRADED COLOR DATA

In order to acquire iris data from large distances and under unconstrained protocols, acceptable depth-of-field values demand high f-numbers for the optical system, corresponding directly (squared) with the amount of light required. Similarly, the motion factor demands very short exposure times, which again augment the amounts of light required. It is known that excessively strong illumination cause permanent eye damage and the NIR wavelength is particularly hazardous, because the eye does not instinctively respond with its natural mechanisms: aversion, blinking, and pupil contraction.

The above points were the major motivations for using visible-light in *in-the-wild* iris biometrics, even though such light spectrum increases the challenges in performing reliable recognition. The pigmentation of the human iris consists mainly of two molecules: brown-black Eumelanin (over 90%) and yellow-reddish Pheomelanin [18]. Eumelanin has most of its radiative fluorescence under the visible wavelength, which —if properly imaged— enables to capture much higher level of detail, but also more noisy artefacts, including specular and diffuse reflections and shadows. In practice, this points for the uniqueness of the iris texture acquired in the visible-light spectrum (in a way similar to the empirically suggested for the near-infrared setup in previous studies [8]), but also stresses the difficulty in obtaining good quality data.

### A. Why Is It So Difficult?

There are four families of factors that affect the quality of iris biometric data not acquired under the classical *stop-*

*and-stare* protocol: A) blur; B) occlusions; C) perspective and D) lighting. By working in a broad range of distances and on moving targets, blurred (A.1) and low-resolution (A.2) images are highly probable. Also, portions of the iris texture are occluded by eyelids (B.1), eyelashes (B.2) and glossy reflections (B.3) from the surrounding environment. Camera-to-subject misalignments may occur, due to subjects gaze (C.1) and pose (C.2). Finally, variations in light intensity (D.1), type (D.2) and incident angles (D.3) reinforce the broadly varying features of this kind of data.

Considering that periocular biometrics uses data not only from the iris but also from the surroundings of the eye (e.g., eyelids, eyebrows, eyelashes and skin), particular attention should be paid to additional data degradation factors, such as (E.1) makeup, (E.2) piercings and (E.3) occlusions (e.g., due to glasses or hair).

### B. State-of-the-art

Concluded in 2011, the *NICE: Noisy Iris Challenge Evaluation* [27] promoted the research about iris recognition in visible-light data. It received over one hundred participations and the best performing teams described their approaches in two special issues of the *Image and Vision Computing*<sup>1</sup> and *Pattern Recognition Letters*<sup>2</sup> journals. This event has set the state-of-the-art recognition performance, having the best algorithm achieved d-prime values above 2.57, area under curve around 0.95 and equal error rates of 0.12. This method (due to Tan *et al.* [36]) is actually a *periocular* recognition algorithm: texton histograms and semantic rules encode information from the surroundings of the eye, while ordinal measures and color histograms analyse the iris. The second best approach was due to Wang *et al.* [38] and is quite more classical: it employs an AdaBoost feature selection scheme from a large set of quantized Gabor-based features, matched by the Hamming distance.

The most relevant recognition algorithms for visible-light images can be divided with respect to their data source: 1)

<sup>1</sup><http://www.sciencedirect.com/science/journal/02628856/28/2>

<sup>2</sup><http://www.sciencedirect.com/science/journal/01678655/33/8>

the iris; or 2) the periocular region. Regarding the first family, Raffei *et al.* [29] preprocessed the iris to remove reflections and represented the normalised data at multiple scales, according to the Radon transform. The score from each scale was matched by the Hamming distance and fused by weighted non-linear combination. Rahulkar and Holambe [31] derived a wavelet basis for compact representation of the iris texture (triplet half-band filters), with coefficients matched by the minimum Cambera distance. A post-classifier outputs a match when more than  $k$  regions give a positive response. Roy *et al.* [30] used a feature selection technique from game theory, based on coefficients from the Daubechies wavelet decomposition. The Hausdorff distance yields the matching score between two feature sets. Kumar and Chan [15] approached the problem from the data representation perspective, having used a quaternionic sparse coding scheme solved by convex optimisation. Quaternion image patches were extracted from the RGB channels and the basis pursuit algorithm used to find the quaternion coefficients. In another work [16], the same authors were based in the sparse representation for classification algorithm, using the output of a local Radon transform as feature space.

The second family of algorithms considers other data beside the iris (sclera, eyebrows and skin texture), and its popularity has been increasing since the work of Park *et al.* [22]. Bharadwaj *et al.* [3] fused a global descriptor (GIST) based on five perceptual dimensions (image naturalness, openness, roughness, expansion and ruggedness) to circular local binary patterns. The Chi-squared distance matched both types of features and a fusion scheme (score level) yielded the final matching value.

Crihalmeanu and Ross [5] used the sclera patterns as biometric trait. The sclera was segmented according to the pixel-wise proportion between the NIR and green channel values. After enhancing the blood vessels by a line filter, SURF, minutiae and correlation-based schemes produced the matching scores that were fused subsequently. Similarly, Zhou *et al.* [39] enhanced the blood vessels in the sclera by Gabor kernels and encoded features by line descriptors. The accumulated registration distance between pairs of line segments yielded the matching score. Also, Oh and Toh [19] encoded the information in the sclera by local binary patterns (LBP) in angular grids, concatenated in a single feature vector. Then, a normalised Hamming distance produced the matching score.

In terms of hybrid approaches, Oh *et al.* [20] combined the sclera to periocular features. Directional features from the former region were extracted by structured random projections, complemented by binary features from the sclera. Tan and Kumar [35] fused iris information (encoded by Log-Gabor filters) to an over-complete representation of the periocular region (LBP, GIST, Histogram of Oriented Gradients and Leung-Malik Filters). Both representations were matched independently and fused at the score level.

Table I overviews the state-of-the-art algorithms in terms of biometric recognition from visible-light ocular data. It compares the analysed traits and summarises the techniques used in segmentation, feature encoding and matching. The error rates reported by authors are also given (*Performance* column).

However, note the above listed algorithms might had used different experimental protocols and data subsets, which turns the direct comparison of the error rates unfair.

### III. STRONG BIOMETRIC TRAIT: IRIS TEXTURE

Motivated by the Daugman's pioneering method [6], there is a tradition of using phase-based techniques to encode iris data: phase is particularly discriminating between irises, if the alignment between gallery and probe samples is guaranteed. We also analyse the iris texture from the phase perspective, with three singularities: 1) to take advantage from the available multi-spectral data, the normalised iris is represented simultaneously in multiple perceptual color spaces; 2) inspired by the concept of ordinal filters [34], we extract not only the sign of coefficients but also consider their magnitude, using a sigmoid transfer function that eliminates the discontinuity of the sign function; and 3) we use a (filter) feature selection algorithm to find the optimal feature set, coming out with a compact yet effective representation of the iris.

#### A. Iris Segmentation and Parameterisation

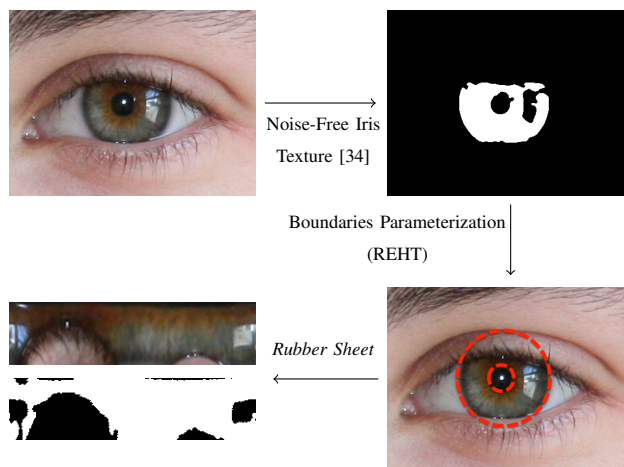


Fig. 2. Processing chain for detecting the noise-free iris regions, parameterizing the iris boundaries and converting data into the polar domain.

There is a classical pattern recognition rule stating that "*weak data should be modelled with strong constraints*" [8]. Accordingly, an extremely robust algorithm for detecting the noise-free iris texture [34] was firstly used (producing the segmentation masks illustrated in the upper-right corner in Fig. 2) and non-concentric ellipses were considered to model the iris boundaries, according to the Random Elliptic Hough Transform (REHT). However, as the segmentation masks have shapes that are usually very far from elliptic, an objective function was designed to post-process the output of the REHT algorithm, and select the pair of ellipses that most likely corresponds to the biological (pupillary and scleric) iris boundaries. This function privileges the centre agreement between both ellipses and near-circular shapes. Let the  $i^{th}$  ellipse (out of  $t_e$ ) be denoted by  $\gamma_i = [x_i, y_i, a_i, b_i, p_i]$ , being  $(x_i, y_i)$  the ellipse centre,  $a_i, b_i$  the major / minor axes

TABLE I  
 STATE-OF-THE-ART ALGORITHMS FOR RECOGNISING DEGRADED OCULAR DATA ACQUIRED IN VISIBLE LIGHT ENVIRONMENTS.

Method	Traits	Segmentation	Feat. Encoding	Feat. Matching	Performance
Bharadwaj <i>et al.</i> [3]	Periocular (Holistic)	-	GIST, CLBP	Chi-square distance	73% rank-1 (UBIRIS.v2)
Crihalmeanu and Ross [5]	Sclera	Green channel vs. NIR intensity	SURF, Minutae (vessel bifurcations)	Euclidean distance, data correlation	EER < 1.8% (Own dataset)
Kumar and Chan [15]	Iris	-	Quaternion Sparse Orientation Code	Shift Alignment	48% rank-1 (UBIRIS.v2)
Kumar <i>et al.</i> [16]	Iris	-	Radon local transform	Sparse Representation for Classification	40% rank-1 (UBIRIS.v2), 33% rank-1 (FRGC)
Oh and Toh [19]	Sclera	HSV space analysis	LBP	Hamming distance	EER 0.47% (UBIRIS.v1)
Oh <i>et al.</i> [20]	Periocular (Holistic), Sclera	Integro-differential operator (iris), HSV color space analysis (sclera)	Multi resolution LBP (Sclera), Directional Projections (Periocular)	Hamming and Euclidean distance	EER 5% (UBIRIS.v2)
Raffei <i>et al.</i> [29]	Iris	Reflection removal, Hough transform	Multi-scale local Radon transform	Hamming distance, weighted non-linear score combination	AUC 88% (UBIRIS.v2)
Rahulkar and Holambe [31]	Iris	-	Triplet half-band filter bank	Canberra distance, k-out-of-n post classifier	Acc > 99% (UBIRIS.v1)
Roy <i>et al.</i> [30]	Iris	Active contours	Daubechies wavelet, Modified Contribution feature selection	Hausdorff distance	TPR 97.43% @ 0.001%FPR (UBIRIS.v1)
Tan and Kumar [35]	Iris, Periocular (Holistic)	Random walker algorithm, edge detection, Hough transform	Log-Gabor filters (Iris), SIFT, GIST, LBP, HOG and LMF (Periocular)	Chi-square and Euclidean distances	39.4% rank-1 (UBIRIS.v2)
Tan <i>et al.</i> [36]	Iris, Eye	-	Texon Histograms, Semantic information (Eye), Ordinal Filters, Color Histogram (Iris)	Chi-square, Euclidean, Diffusion and Hamming distances	AUC 95%(UBIRIS.v2)
Wang <i>et al.</i> [38]	Iris	-	Gabor filters, AdaBoost feature selection	Hamming distance	AUC 88% (UBIRIS.v2)
Zhou <i>et al.</i> [39]	Sclera	HSV color space analysis, dynamic thresholding, convex hull analysis	Line (sclera vessels) description	Accumulated line registration cost	EER 3.83% (UBIRIS.v2)

and  $p_i$  the REHT score (the proportion of edge pixels in the segmentation mask that overlap  $\gamma_i$ ). For  $\binom{t_e}{2}$  pairs, the following objective function gives their goodness:

$$J(\gamma_i, \gamma_j) = \left[ \frac{\| (x_i, y_i) - (x_j, y_j) \|_2}{\max(a_i, a_j)}, \frac{a_i - b_i}{a_i} + \frac{a_j - b_j}{a_j}, p_i + p_j \right] \cdot [\alpha_1, \alpha_2, \alpha_3]^T, \quad (1)$$

being  $\alpha_i$  regularisation terms ( $\alpha_1, \alpha_2 < 0, \alpha_3 > 0$ ). The deemed iris boundaries correspond to:

$$(\gamma_i^*, \gamma_j^*) = \arg \max_{i,j} J(\gamma_i, \gamma_j). \quad (2)$$

Converting the segmented data into a dimensionless pseudo-polar coordinated system (Daugman's *rubber sheet* model) yields a set of normalised iris images and of segmentation masks that discriminate between the occluded and noise-free iris pixels (bottom-left images in Fig. 2). This enabled to obtain segmented images that were considered plausible (under visual inspection) in 92.60% for the UBIRIS.v2 and 95.40% for the FRGC data sets. The noise-free iris texture detection algorithm due to Tan *et al.* [36] proved to be remarkably effective against the typical data covariates (pose, gaze, iris occlusions and dynamic lighting conditions), which turned easier the tasks of the REHT and Rubber Sheet phases. Also, the most problematic

case occurred in images severely occluded by eyelids where the pupillary and scleric boundaries are connected, which biased the results of REHT and, necessarily, of the Rubber Sheet phase.

However, in order to avoid that errors in segmentation bias the subsequent processing phases, and to perceive the strengths / weaknesses of the proposed ensemble, we filtered the wrongly / inaccurately segmented images and guaranteed that all images used in Section V were segmented in a plausible way.

### B. Preliminary Selection of Color Spaces

To exploit the multi-spectral information available in visible-light images, they were represented in various perceptual color spaces, summarised in Table II (details about the conversions are given in [32]). However, all these representations combined with the filter parameterisations lead to an intractable feature set. Hence, the data variability per color channel was assessed, and only a subset of the channels was considered for further processing, according to the concept of *eigeniris*. Let  $t$  be the number of images  $\mathbf{I}$  in a learning set, each one represented as a  $n$ -length column vector. Let  $\bar{\mathbf{I}} = \frac{1}{t} \sum \mathbf{I}_i$  be the mean image,  $\mathbf{D}_i = \mathbf{I}_i - \bar{\mathbf{I}}$  the residuals and  $\mathbf{A} = [\mathbf{D}_1, \dots, \mathbf{D}_t]$  their concatenation ( $n \times t$  matrix). Obtaining the eigenvectors of  $\mathbf{A}$  requires to work with  $\mathbf{A}\mathbf{A}^T$ , which has an intractable dimension. Let  $\mathbf{A}^T \mathbf{A}$  be a  $t \times t$  matrix and  $\mathbf{v}_i$  ( $i \in \{1, \dots, t\}$ ) its eigenvectors. Then,

TABLE II  
 SUMMARY OF THE PERCEPTUAL COLOR REPRESENTATIONS USED TO ENCODE VISIBLE-LIGHT IRIS DATA.

Col. Sp.	Conversion (from RGB)	Description
<b>RGB</b>	—	No invariance properties
<b>HSV</b>	Algorithm described in [1]	Cylindrical-coordinate representations of points in RGB.
<b>XYZ</b>	Algorithm described in [37]	Using $2^{nd}$ observer, D65 illuminant.
<b>LAB</b>	Algorithm described in [13]	Using $2^{nd}$ observer, D65 illuminant. Close to perceptual uniformity.
<b>RG</b>	$\begin{pmatrix} R \\ G \end{pmatrix} = \begin{pmatrix} \frac{R}{R+G+B} \\ \frac{G}{R+G+B} \end{pmatrix}$	Uses the normalised RGB color model ( $R+G+B=1$ ). R and G are invariant to light intensity.
<b>T-RGB</b>	$\begin{pmatrix} R \\ G \\ B \end{pmatrix} = \begin{pmatrix} \frac{R-\mu_R}{\sigma_R} \\ \frac{G-\mu_G}{\sigma_G} \\ \frac{B-\mu_B}{\sigma_B} \end{pmatrix}$	Invariant to scale and shift with respect to light intensity. Normalised against changes in light color and arbitrary offsets.
<b>O-RGB</b>	$\begin{pmatrix} O_1 \\ O_2 \\ O_3 \end{pmatrix} = \begin{pmatrix} \frac{R-G}{\sqrt{2}} \\ \frac{R+G-2B}{\sqrt{6}} \\ \frac{R+G+B}{\sqrt{3}} \end{pmatrix}$	Based in the opponent color space. Intensity is represented in $O_3$ channel and color in $O_1$ and $O_2$ channels that are shift-invariant with respect to light intensity.

$$\mathbf{A}^T \mathbf{A} \mathbf{v}_i = \lambda_i \mathbf{v}_i. \quad (3)$$

Multiplying both sides by  $\mathbf{A}$ , we have:

$$\mathbf{A} \mathbf{A}^T (\mathbf{A} \mathbf{v}_i) = \lambda_i (\mathbf{A} \mathbf{v}_i), \quad (4)$$

concluding that  $\mathbf{A} \mathbf{v}_i$  are eigenvectors of  $\mathbf{A} \mathbf{A}^T$ . The *eigenirises*  $\mathbf{u}_i$  are given by  $\mathbf{u}_i = \mathbf{v}_i \mathbf{A}$  and their magnitude gives the data variability in a color channel. Fig. 3 illustrates this concept by displaying (at the bottom histogram) the accumulated magnitude of the principal *eigenirise*  $\mathbf{u}_1$  of each color channel (note that intensities are stretched for visualisation purposes). The bar plot at the top accumulates the magnitudes of the top-10 *eigenirises*, i.e., those associated with the largest eigenvalues. This plot highlights the variations among color channels: the RGB, Opposite-RGB, and intensity channel of HSV carry the predominating orthogonal variability, followed by the XYZ and  $L^*AB$ . In opposition, the RG and Transformed-RGB spaces had such small accumulated magnitudes that were disregarded from the subsequent phases of this work.

### C. Feature Encoding

The iris codes were extracted by convolving the normalised data with a bank of Multi-Lobe Differential Filters (MLDF), recently reported as a relevant advance to the iris recognition field [33]. They are expressed in terms of the number of lobes, location, scale, orientation and inter-lobe distance. To keep the number of possibilities tractable, only filters with Gaussian kernels and equal number and scale of positive / negative lobes ( $1/1, 2/2, \dots$ ) were considered:

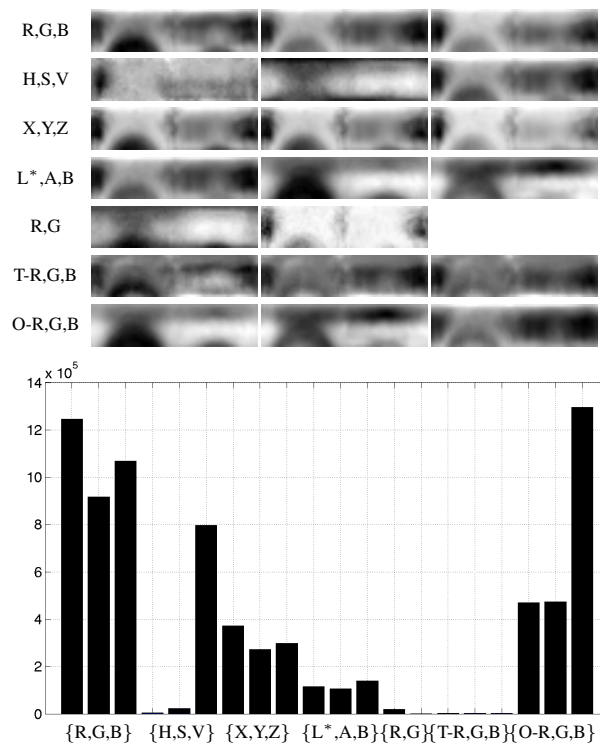


Fig. 3. Top plot: Magnitude of the first eigenvector of each color channel (note that intensities are stretched for visualisation purposes). The bottom plot is the accumulated magnitude of the top-10 eigenvectors per color channel.

$$\mathbf{m}[\mathbf{x}_j, \mu_j, \sigma_j] = \sum_{j=1}^l (-1)^{j+1} \frac{1}{\sqrt{2\pi\sigma_j}} \exp \left[ \frac{-(\mathbf{x}_j - \mu_j)^2}{2\sigma_j} \right], \quad (5)$$

being  $\mathbf{x}_j = (x_j, y_j)$  the center of each lobe and  $l$  the number of lobes. Fig. 4 illustrates examples of MLDFs, with varying number of lobes, scales and inter-lobes distances  $d$ .

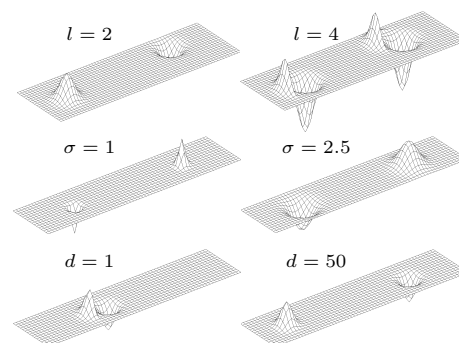


Fig. 4. Examples of the filters used by the iris biometric expert, displaying varying number of lobes (top row), sigmas (middle row) and inter-lobes distance (bottom row).

To attenuate the reduced data resolution and amount of information available, not only the sign of the  $\mathbf{I} * \mathbf{m}$  coefficients was considered but also their weighted magnitude. A transfer

function with sigmoid shape was designed, mapping large magnitude values to 0/1, but also values near the vertical axis to the unit interval. This way, even considering values near the vertical axis as less reliable, it was accounted that they should contain *some* discriminating information and were still considered in the matching process, with a smaller weight than for large magnitude values. According to this idea, the  $\ell_2$  norm was used as matching function between two iris codes. Fig. 5 compares the traditionally used sign-based strategy for codes quantisation (continuous line) and the proposed variant (dashed line). The horizontal axis corresponds to the values of  $I * m$  and the vertical axis gives the corresponding weight in the matching process. It can be seen that, in both strategies, values with magnitude above  $\nu$  are mapped equally to the  $\{0,1\}$  values.

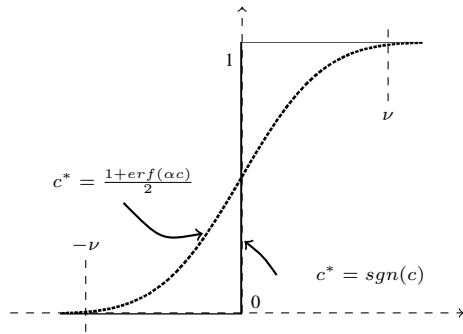


Fig. 5. Comparison between the traditionally used sign-based function for codes quantisation (continuous line) and the sigmoid function used in this paper (dashed line).

#### D. Learning Phase

The Sequential Floating Feature Selection (SFFS) algorithm [28] was used to select the best combination of features in a learning set. Other alternatives, such as the Fisher-score [11] and the Minimum Redundancy - Maximum Relevance (mRMR) algorithm [23] were tested, having obtained the following AUC values and corresponding 95% confidence intervals:  $0.781 \pm 0.020$  (Fisher),  $0.713 \pm 0.018$  (mRMR) and  $0.950 \pm 0.017$  (SFFS) for the UBIRIS.v2 dataset and  $0.815 \pm 0.016$  (Fisher),  $0.860 \pm 0.016$  (mRMR) and  $0.951 \pm 0.018$  (SFFS) for the FRGC. The values were obtained by selecting iteratively random samples of 90% of the available learning data and using the remaining 10% pairwise comparisons for performance evaluation.

According to these results, the SFFS algorithm was considered the most appropriate, with the following objective function:

$$J(\{f, \mathcal{S}\}) = \frac{\sqrt{2} |\mu_{H_0}^{\{f, \mathcal{S}\}} - \mu_{H_a}^{\{f, \mathcal{S}\}}|}{\sqrt{(\sigma_{H_0}^{\{f, \mathcal{S}\}})^2 + (\sigma_{H_a}^{\{f, \mathcal{S}\}})^2}}, \quad (6)$$

being  $f$  a candidate feature,  $\mathcal{S}$  the set of selected features,  $\mu$  and  $\sigma$  the mean and standard deviations of the  $\ell_2$  norm between two feature vectors. The subscript denotes the class ( $H_0$

represents genuine comparisons) and  $\{.,.\}$  is the concatenation operator. Starting with the empty set  $\mathcal{S} = \emptyset$ , at each iteration the best feature was taken:  $f^* = \arg_i \max J(\{f_i, \mathcal{S}\})$  and added to the selected set  $\mathcal{S} \doteq \{\mathcal{S}, f^*\}$ . After each insertion, the exclusion of features previously selected was considered:  $f^* = \arg_i \max J(\{\mathcal{S} \setminus f_i\})$ , where " $\setminus$ " denotes set complement. If  $J(\{\mathcal{S} \setminus f^*\}) > J(\mathcal{S})$ ,  $f^*$  was excluded from  $\mathcal{S}$ .

#### IV. WEAK BIOMETRIC TRAIT: EYELIDS, EYELASHES AND SKIN

This section describes a biometric expert that analyses the surroundings of the human eye. The process is based in the segmentation of the iris and of the eyelids boundaries, defining a dimensionless ROI from where shape and texture descriptors are extracted. This ends up with an expert that is considered *weak*, in the sense that it cannot be used alone to reliably identify a subject, but is particularly useful to complement an iris biometric expert, due to its low correlation and reduced sensitivity to the most problematic iris data covariates.

##### A. Sclera Detection

The sclera can be detected at the pixel level [26], using as discriminating features the hue  $h$  and saturation  $s$  channels of the HSV color space, and the red  $cr$  and blue chroma  $cb$  values of the yCbCr space (Fig. 6). Geometrical information (angle and distance) of each position in the image with respect to the iris center of mass and major chord may also be helpful (the sclera is adjacent to the iris and spreads in opposite directions with respect to it), yielding a feature vector  $[h_i, s_i, cr_i, cb_i, \rho_i, \theta_i]$ ,  $\rho_i = \|(x_i, y_i) - (c_x, c_y)\|_2$ ,  $(c_x, c_y)$  is the iris centre of mass and  $\theta_i = \arctan(|y_i - c_y, x_i - c_x|)$ .

A binary non-linear classification model (feed-forward neural network) was learned, being its output illustrated in the upper-right corner of Fig. 6. Next, morphologic operators smoothed the output of the classifier and only the two largest connected components were kept.

##### B. Eyelids Parameterisation

Let  $\mathbf{M} = \mathbf{B} \oplus \mathbf{S}$  be a mask combining the segmented iris  $\mathbf{B}$  and sclera  $\mathbf{S}$  ( $\oplus$  is the bitwise-or operator). Let  $\mathbf{E} = \{(x_i, y_i)\}$  be the set of  $t$  edge pixels in  $\mathbf{M}$  (ordered clockwise) and  $l^* = \arg \min_i x_i$ ,  $r^* = \arg \max_i x_i$  the deemed positions of the eye corners.  $\mathbf{E}$  can be divided into two subsets with indexes  $e^{(1)} : \{l^*, \dots, r^*\}$  and  $e^{(2)} : \{r^*, \dots, t, 1, l^*\}$ , each one representing one of the eyelids. The following system of linear equations finds the coefficients of an interpolating polynomial of degree  $n$ :

$$\begin{bmatrix} x_{e_0}^n & x_{e_0}^{n-1} & \dots & x_{e_0}^0 \\ x_{e_1}^n & x_{e_1}^{n-1} & \dots & x_{e_1}^0 \\ \vdots & \vdots & \ddots & \vdots \\ x_{e_n}^n & x_{e_n}^{n-1} & \dots & x_{e_n}^0 \end{bmatrix} \begin{bmatrix} a_0 \\ a_1 \\ \vdots \\ a_n \end{bmatrix} = \begin{bmatrix} y_0 \\ y_1 \\ \vdots \\ y_n \end{bmatrix}, \quad (7)$$

being  $e_i$  an element of  $e^{(\cdot)}$ . The system above finds a solution in the least-squares sense, which most times is not acceptable due to the degradation of the masks  $\mathbf{M}$  from where

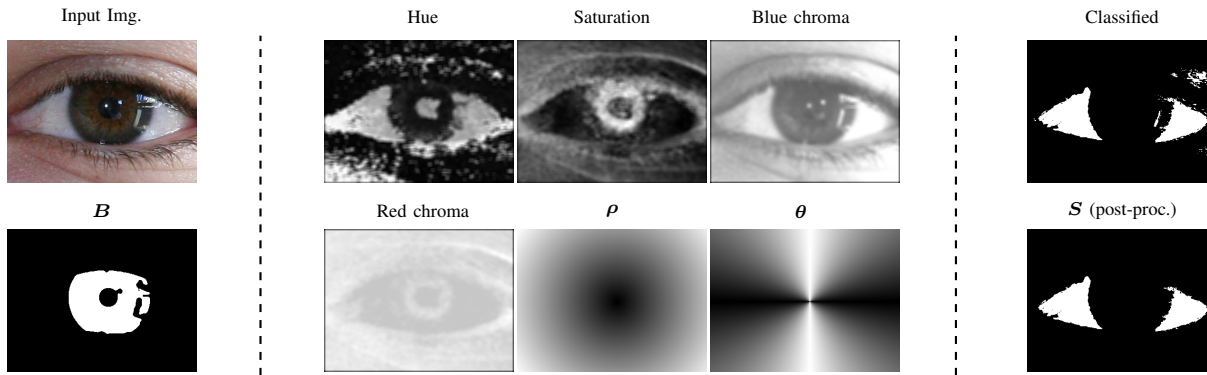


Fig. 6. Phases of the sclera detection method. Using a feature set composed by image hue, saturation, blue and red chroma, the distance  $\rho$  and angle  $\theta$  of each pixel to the iris centre of mass and major chord, a non-linear classifier detects the sclera pixels. Morphologic operators and analysis of connected components yields the result.

$e^{(\cdot)}$  are found. Instead, according to a RANSAC-like strategy, random samples of  $n + 1$  distinct points in  $e$  were drew and a polynomial fitted to each sample (7). Every point was tested against that polynomial and in case it fits *relatively well* the model ( $\ell_2$  distance less than a threshold), its score was incremented (8) by a unit value. At the end, points with scores  $\phi$  near the maximum value were considered inliers and the final polynomial found by least squares minimisation of inliers.

$$\phi^{(t+1)}(i) = \begin{cases} \phi^{(t)}(i) + 1, & \text{if } \|y_i - \sum_{j=0}^n a_j x_i^{n-j}\|_2 < \delta \\ \phi^{(t)}(i), & \text{otherwise} \end{cases}, \quad (8)$$

being  $\delta \approx 1$  used in our experiments.

The next phase comprises the definition of the dimensionless ROI around the visible cornea. Let  $d_c = \|r^* - l^*\|_2$  be the distance between the eye-corners,  $\delta_x = \frac{d_c}{w_e}$ ,  $\delta_y = \delta_x \frac{h_e}{w_e}$ , and  $(h_e, w_e)$  the dimensions of the normalised ROI. Data were sampled from the Cartesian space according to the coordinates:

$$\begin{cases} x_{ik} = x_i + k\delta_x v_i^{(x)}, \\ y_{ik} = \sum_{j=0}^n a_j x_i^{n-j} + k\delta_y v_i^{(y)} \end{cases}, \quad (9)$$

for  $k \in \{1, \dots, h_e\}$ ,  $i \in \{1, \dots, w_e\}$ ,  $\vec{v}_i = (v_i^{(x)}, v_i^{(y)})$  is the unit vector normal to the polynomial at  $(x_i, \sum_{j=0}^n a_j x_i^{n-j})$ . Fig. 7 illustrates this procedure: the leftmost column gives the initial image and, from left to right, its mask  $M$  and the polynomial parameterisations (red curves) are shown. Also, the ROIs around the eyelids are plotted in the Cartesian and dimensionless normalised spaces.

### C. Feature Encoding and Matching

Two families of feature descriptors were considered: 1) Shape; to characterise the polynomial of each eyelid; and 2) Texture; to encode information in the ROIs.

1) *Shape Descriptors*: The local accumulated curvature at the  $i^{th}$  point (out of  $t$ ) in the eyelids boundary is given by  $\sum_{j=1}^i \frac{\partial^2 y_j}{\partial x^2} / \sum_{j=1}^t \frac{\partial^2 y_j}{\partial x^2}$ . Also, the shape context proposed by Belongie *et al.* [2] efficiently measures the similarity between shapes. For each  $(x_i, y_i)$ , a histogram  $h_i$  of  $(x_i - x_j, y_i -$

$y_j), \forall j \neq i$  was represented in log-polar coordinates. The cost of matching  $h_i$  with  $h_j$  uses the  $\chi^2$  statistic:

$$R_{ij} = \frac{1}{2} \sum_{k=1}^K \frac{(h_i(k) - h_j(k))^2}{h_i(k) + h_j(k)}, \quad (10)$$

where  $h_i(k)$  denotes the  $k^{th}$  bin of the histogram. The set of all costs  $R_{ij}$  between pairs of points was regarded as the cost matrix of a bipartite graph-matching problem and solved by a linear assignment algorithm.

Based in the work of Mallat and Zhang [17],  $\mathbf{y} = \{y_1, \dots, y_n\}$  was considered a time-dependent 1D signal and decomposed into a linear expansion of signals taken from an over-complete dictionary:

$$\mathbf{y} = \sum_i a_i g_{\gamma^*}, \quad (11)$$

being  $g_{\gamma}$  the dictionary atoms and  $a_i$  the weighting factors. At each iteration, the atom  $g_{\gamma^*}$  that maximally correlates  $\mathbf{y}$  was subtracted from a residual, i.e.,  $r^{(t+1)} = r^{(t)} - a_n g_{\gamma^*}$ . The process iterates until the  $\ell_\infty$  norm of the residual is smaller than a threshold. The resulting  $\mathbf{a}$  values were matched by the  $\chi^2$  statistic (10).

Finally, Elliptical Fourier Descriptors [12] parameterise the  $\mathbf{y}$  coordinates by:

$$y_t = \sum_{i=0}^{\infty} [a_i, b_i] \left[ \cos\left(\frac{2i\pi t}{T}\right), \sin\left(\frac{2i\pi t}{T}\right) \right]^T, \quad (12)$$

being  $a_0 = 0$ ,  $b_0 = \frac{1}{T} \int_0^T y(t) dt$ ,  $a_i = \frac{2}{T} \int_0^T y(t) \cos\left(\frac{2i\pi t}{T}\right) dt$  and  $b_i = \frac{2}{T} \int_0^T y(t) \sin\left(\frac{2i\pi t}{T}\right) dt$ .

2) *Texture Descriptors*: Proposed by Ojala *et al.* [21], Local Binary Patterns (LBP) are among the most popular texture descriptors in the literature. The LBP value of an image pixel is actually a binary representation of the position of its neighbours with higher intensity, i.e.,  $f_{lbp}(x, y) = \sum_{p=0}^{t_p} s(I(x, y) - I(x', y')) 2^p$ , being  $s(\cdot)$  the Heaviside step function and  $(x', y')$  the coordinate of the  $t_p$  neighbours in a circular path. Histograms of the  $f_{lbp}$  values in image patches were concatenated and matched by the  $\chi^2$  statistic (10).

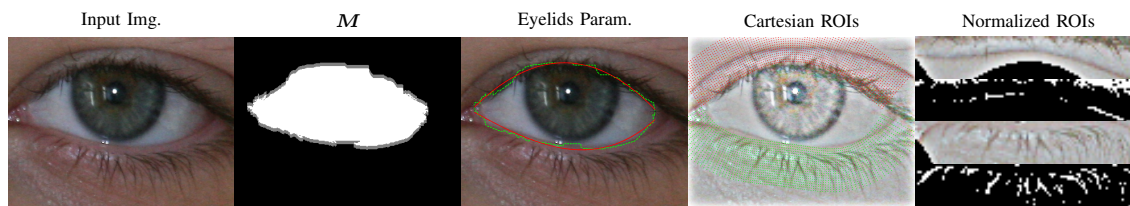


Fig. 7. Example of a eyelids parameterisation (red curve in 'Eyelids Param. '), according to the boundary of the binary  $M$  masks. The right images give the regions-of-interest in the Cartesian and dimensionless normalised spaces.

## V. EXPERIMENTS AND DISCUSSION

### A. DataSets

Two freely available sets of visible-light data were used in the empirical evaluation:

- The UBIRIS.v2 [25] has 11,102 images, acquired between three and eight meters away from 261 subjects, under dynamic lighting and unconstrained setups. Images have glossy reflections in the iris, occlusions due to eyelids and eyelashes, off-angle and blurred data. 2,340 images were selected, having manually confirmed the plausibility of the corresponding iris segmentation.
- The FRGC [24] is mainly a data source for face recognition and, as such, images have limited resolution. The still images subset from the controlled / uncontrolled setups was used, comprising frontal images with shadows and glossy reflections occluding portions of the irises. 4,360 images were selected, all having the iris accurately segmented.



Fig. 8. Examples of the data used in the experimental evaluation. The upper rows are from the UBIRIS.v2 and the bottom rows from the FRGC dataset.

A large set of pairwise comparisons was randomly selected as learning data (20,000 genuine and 20,000 impostor comparisons per data set) and completely disjoint sets of 50,000 genuine and 250,000 impostor comparisons were used to evaluate performance.

### B. Baseline Algorithms

Four algorithms were considered as comparison terms, based in their relevance in the literature. 1) the first is due to Tan *et al.* [36], and got the best performance in the NICE contest (section II-B); 2) the runner-up approach of NICE, due to

Wang *et al.* [38] (section II-B); 3) a variant of the Daugman's recognition algorithm [9], extracting a set of Gabor features from the normalised iris data, pruned by a sequential feature selection method. 4) the most well known periocular recognition algorithm, due to Park *et al.* [22]. It uses the centre of the iris to define a region-of-interest where a  $5 \times 7$  grid is superimposed. Local feature extraction is carried out by LBPs and HOGs. Global information of the ocular region is encoded by the Scale Invariant Feature Transform (SIFT). All types of features are fused at the score level.

### C. Fusion of Strong / Weak Experts

This section addresses the variations in performance attained by fusing (at the score level) the two kinds of experts proposed. We start by illustrating (Fig. 9) the decision environment for each feature of the weaker expert considered individually, displaying the probability density functions obtained for the genuine (continuous lines) and impostor (dashed lines) pairwise comparisons. It is evident that texture descriptors are more effective than shape descriptors, and the lower eyelid provides more discriminating information in terms of shape than the upper eyelid, probably due to its smaller amplitude of movements. In this case, the movements of the *levator palpebrae superioris* muscle augment the variability in shape of the upper eyelid, which might had contributed for its smaller discriminability. Note that the features displayed here were those that optimised the performance of a neural network classifier. Even though some appear to be poor, they provide valuable complementary information with respect to others.

Next, using the theoretical framework developed by Kittler *et al.* [14], combinations of the strong and weak experts were tested, according to the usual fusion rules: *product*, *sum*, *min* and *max*. We adopt the notation used by Bolle *et al.* [4]. Having two iris codes  $c^{(p)}$ ,  $c^{(q)}$ , the null hypothesis  $H_0$  is that they were extracted from images of the same eye. The alternative hypothesis  $H_a$  is that they regard different eyes. Without any assumption on the prior probabilities, the posterior probability that  $c = \|c^{(p)} - c^{(q)}\|_2$  belongs to class  $H_0$  is given by:

$$P(H_0|c) = \frac{P(c|H_0)}{P(c|H_0) + P(c|H_a)}. \quad (13)$$

An input pattern was assigned to class  $H_j$  when  $j = \arg_i \max_\phi P(H_i|c)$ , being  $\phi$  the combination rule and  $i \in \{0', a'\}$ . Fig. 10 expresses the effectiveness of each fusion rule, concluding that the *sum* of posteriors led to the best performance, consistently above the strong baseline expert. The

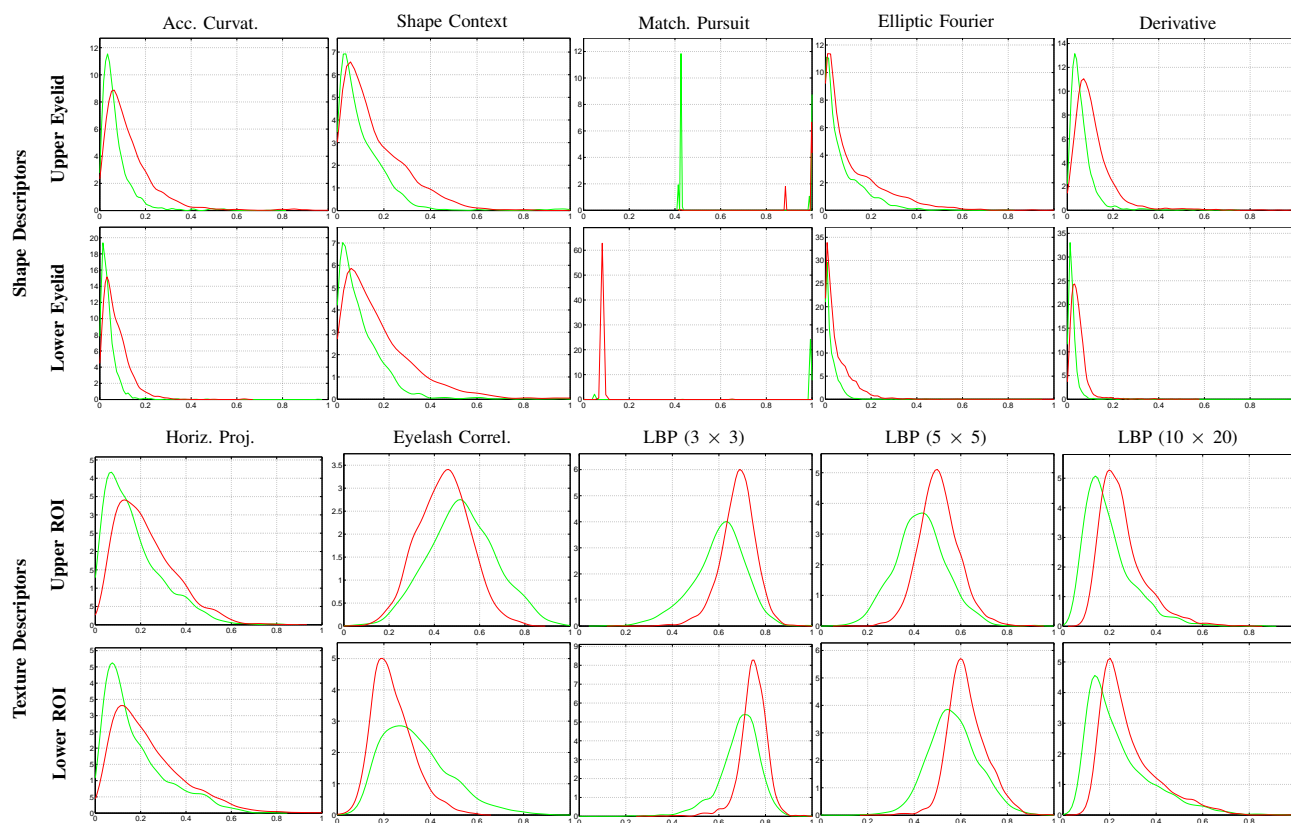


Fig. 9. Density functions for each feature of the weak biometric expert considered individually (UBIRIS.v2 dataset). The green lines regard genuine pairwise comparisons and the red lines are from impostors comparisons. Most of the discriminating information is on the texture descriptors from the dimensionless ROI. Shape descriptors mostly provide complementary information.

*max* and *min* rules produced classifiers with performance close to the strong classifier and the *product* rule led to the worst results.

To conclude this section, and to illustrate the actual advantages attained by fusing the two types of experts described in this paper, in Fig. 11 we compare the performance attained by two strong (iris) and a strong / weak (ocular) experts. We show a strong expert  $S_1$ . Then, other strong (iris) experts  $S_2$  working on a completely disjoint feature set from  $S_1$  ( $S_1 \cap S_2 = \emptyset$ ) was obtained, but was observed to produce responses highly correlated to  $S_1$  (due to the fact that both are particularly sensitive to the same image covarites: gaze, pose, lighting and occlusions). On the other way,  $W$  is a weak expert with substantially worse performance than  $S_1$  and  $S_2$ . Even though, more evident improvements are observed for the  $S_1 + W$  case than for  $S_1 + S_2$ , confirming the important rule of linear correlation  $r(\cdot)$  in fusion:  $r(S_1, S_2) = 0.979$ ,  $r(S_1, W) = 0.017$  in the UBIRIS.v2 and  $r(S_1, S_2) = 0.969$ ,  $r(S_1, W) = 0.019$  in the FRGC set.

#### D. State-of-the-Art: Performance Comparison

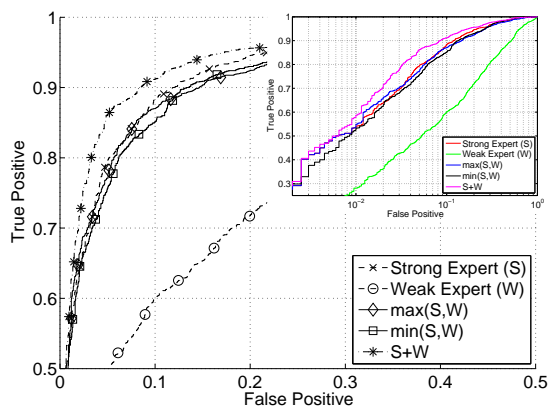
Fig. 12 contextualises the effectiveness of the proposed ensemble with respect to the state-of-the-art, in the UBIRIS.v2 (left plot) and FRGC (right plot) datasets. In both cases, improvements in performance are evident, and occurred in all regions of the performance space. The runner-up methods

were Tan *et al.* (UBIRIS.v2) and the Wang *et al.* (FRGC). The classical Gabor-based decomposition of the iris texture got between third and fourth rank, whereas the poorest performance was observed for the Park *et al.*'s method, which most times was due to errors in the definition of the ROIs. This method uses the centre of the iris as reference point, and in many cases our images have deviated gazes, which might had biased all the subsequent processing.

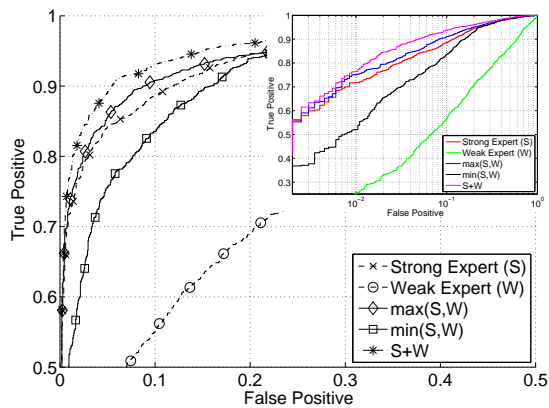
The effectiveness of the ensemble is particularly evident from the comparison of summary measures: area under curve (AUC) values of 0.965 for our method, followed by 0.946 for the Tan *et al.* algorithm, 0.882 for the Wang *et al.*, 0.872 for the Daugman and 0.846 for the Park *et al.* (UBIRIS.v2 dataset). Regarding the FRGC set, the performance rank of each algorithm was similar, with exception to the method of Tan *et al.* that substantially decreased its performance (AUC of 0.973 for the proposed method, 0.913 for Tan *et al.*, 0.948 for Wang *et al.*, 0.900 for Daugman and 0.772 for Park *et al.*). The recognition effectiveness is summarised in Table III. The experiments were repeated 20 times, using random samples composed by 90% of the probe pairwise comparisons, being plotted the mean and the standard deviation observed.

#### E. When Should Not the Ensemble Be Used?

The substantial decreases in performance of the Tan *et al.* and Park *et al.* methods in the FRGC dataset were the subject



UBIRIS.v2



FRGC

Fig. 10. Recognition performance of the ensemble with respect to the strong  $S$  and weak  $W$  experts considered individually.

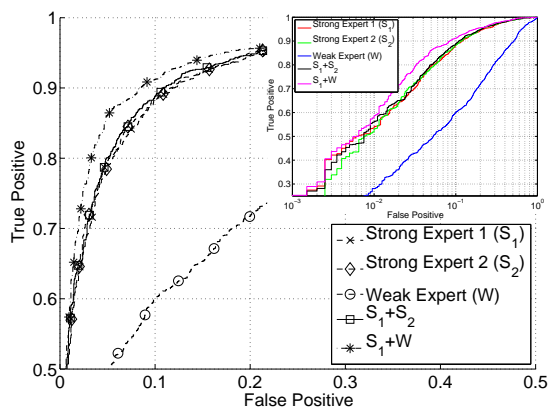
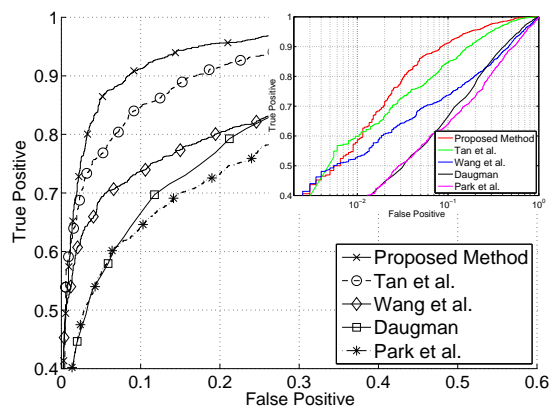
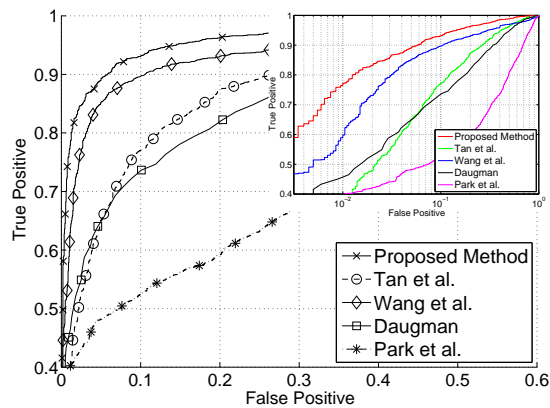


Fig. 11. Improvements in performance due to the fusion of a strong expert  $S_1$  and a quasi-independent poor expert  $W$  are much more evident than when fusing two heavily correlated strong experts  $S_1, S_2$ .

of further analysis. We noticed that the FRGC images used in our experiments were cropped such that the eyebrows are rarely visible, and much less skin is visible than in the UBIRIS.v2. As both algorithms belong to the *periocular* recognition family, the most valuable information they extract is from the skin surrounding the eye and from the shape of eyebrows.



UBIRIS.v2



FRGC

Fig. 12. Comparison between the recognition effectiveness obtained by the ensemble proposed in this paper, with respect to the state-of-the-art algorithms. Results regard the UBIRIS.v2 (top plot) and FRGC (bottom plot) datasets.

TABLE III  
SUMMARY OF THE PERFORMANCE MEASURES OBSERVED FOR THE UBIRIS.v2 AND FRGC DATASETS.

Method	UBIRIS.v2		FRGC	
	$d'$	AUC	$d'$	AUC
Proposed Ensemble	$2.97 \pm 0.04$	$0.965 \pm 0.002$	$3.02 \pm 0.03$	$0.973 \pm 0.001$
Strong Expert (Individually)	$2.85 \pm 0.04$	$0.950 \pm 0.001$	$2.87 \pm 0.03$	$0.951 \pm 0.001$
Weak Expert (Individually)	$1.63 \pm 0.05$	$0.720 \pm 0.003$	$1.78 \pm 0.04$	$0.759 \pm 0.003$
Tan <i>et al.</i>	$2.57 \pm 0.04$	$0.946 \pm 0.001$	$2.25 \pm 0.04$	$0.913 \pm 0.002$
Wang <i>et al.</i>	$1.82 \pm 0.03$	$0.882 \pm 0.001$	$2.79 \pm 0.03$	$0.948 \pm 0.001$
Daugman (Gabor)	$1.81 \pm 0.04$	$0.872 \pm 0.001$	$2.02 \pm 0.03$	$0.900 \pm 0.001$
Park <i>et al.</i>	$1.76 \pm 0.05$	$0.846 \pm 0.001$	$1.65 \pm 0.03$	$0.772 \pm 0.001$

To perceive the effect of this factor as a covariate, the experiments in the FRGC dataset were repeated using wider periocular regions, which produced the results given in Fig. 13. Picking the best algorithm, it can be seen that the Tan *et al.*'s method substantially increased its performance when wider areas around the eye were available, whereas our ensemble

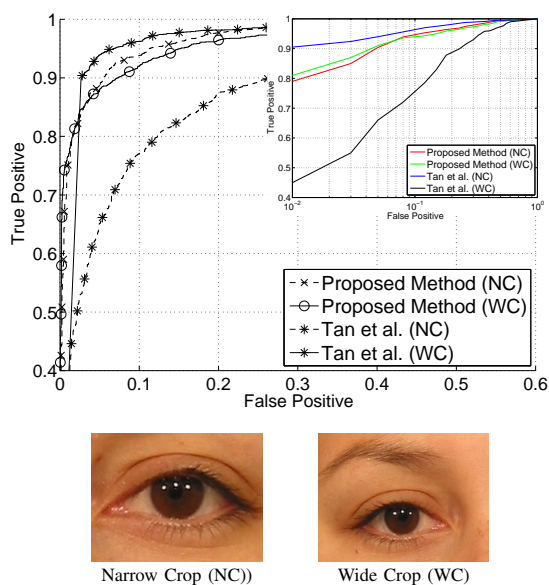


Fig. 13. Variations in recognition effectiveness with respect to the wideness of the region available nearby the eye.

remained approximately invariant to this factor. Hence, the conclusion is that the method due to Tan *et al.* is better than ours when the area available covers the eyebrows and wide regions of the surrounding skin. This was not particularly surprising as we decided not to encode any type of information from the eyebrows, as they can be easily changed by anyone not willing to be recognised.

As concluding remark, Fig. 14 illustrates the rationale of the proposed recognition ensemble, displaying pairwise image comparisons of the UBIRIS.v2 (upper rows) and FRGC datasets (bottom rows), where the strong expert had high uncertainty (posteriors  $P_s \approx 0.5$ ) in discriminating between the genuine (framed by green rectangles) and impostor comparisons (red rectangles). For genuine comparisons, it can be seen that differences in scale (cells A.1 and A.2), harden the matching process, as do gaze deviations (A.3) and iris occlusions (C.2). However, the most common factor observed to deteriorate the scores of genuine comparisons was the differences in lighting, as happened in the cells A.2, C.3, C.4, and C.1. Regarding the impostor comparisons, they tend to fall in the uncertainty region when both images have similar levels of iris pigmentation (B.I, B.3, B.4, D.1, D.2 and D.4), similar gaze (B.2 and B.3) and irises are significantly occluded (B.4, D.2 and D.3). In these cases, the posteriors given by the weak expert  $P_w$  were a valuable contribution for better recognition responses, as the weak expert is almost insensitive to factors known that decrease the effectiveness of the iris expert, as occlusions, gaze and changes in illumination. It should be noted that — actually — this is the main insight behind the ensemble proposed: provide two practically independent experts that are also sensitive to disjoint image covariates.

## VI. CONCLUSIONS

As an attempt to improve the biometrics performance on degraded ocular data, this paper describes an ensemble

composed by two experts that work on fully disjoint data and were designed to produce quasi-independent responses. A *strong* expert (iris) analyses the iris texture based on multi-lobe differential filters and considers both the signal phase and magnitude, in order to augment the amount of discriminating information. Complementary, a *weak* expert (ocular) analyses the shape of eyelids, the geometrical features of the eyelashes and of the skin furrows nearby the cornea.

By fusing both experts at the score level, we observed consistent improvements with respect to the strongest expert, simultaneously in terms of recognition effectiveness and robustness. This was justified by three important features of the ensemble: 1) the linear correlation between the responses given by both experts is residual (less than 0.02), which accounts for the recognition effectiveness; 2) the iris and ocular experts are not sensitive to the same image covariates, which accounts for the recognition robustness; 3) both experts avoid to analyse data that can be easily forged (e.g., shape of eyebrows), which can be regarded as an active anti-counterfeiting measure.

Our results were obtained in publicly available data sets and advance considerably the state-of-the-art in terms of ocular recognition in visible-light degraded data, improving the d-prime index over 12% in the UBIRIS.v2 dataset and 8% in the FRGC data set.

## REFERENCES

- [1] M. Agoston. Computer Graphics and Geometric Modeling: Implementation and Algorithms. Springer, pag. 300-306, ISBN: 1-85233-818-0, 2005.
- [2] S. Belongie, J. Malik and J. Puzicha. Shape Matching and Object Recognition Using Shape Contexts. *IEEE Transactions on Pattern Analysis and Machine Intelligence*, vol. 24, no. 24, pag. 509–521, 2002.
- [3] S. Bharadwaj, H. Bhatt, M. Vatsa and R. Singh. Periocular biometrics: When iris recognition fails. in Proceedings of the *International Conference on Biometrics: Theory, Applications and Systems*, pag. 1–6, 2010.
- [4] R.M. Bolle, S. Pankanti, J.H. Connell and N. Ratha. Iris Individuality: A Partial Iris Model. Proceedings of the *17th International Conference on Pattern Recognition*, vol. 2, pag. 927–930, 2004.
- [5] S. Crialmeanu and A. Ross. Multispectral scleral patterns for ocular biometric recognition. *Pattern Recognition Letters*, vol. 33, no. 14, pag. 1860–1869, 2012.
- [6] J. Daugman. High Confidence Visual Recognition of Persons by a Test of Statistical Independence. *IEEE Transactions on Pattern Analysis and Machine Intelligence*, vol. 15, no. 11, pag. 1148–1161, 1993.
- [7] J. Daugman. Biometric decision landscapes. *University of Cambridge Technical Report*, UCAM-CL-TR-482, ISSN: 1476-2986, 2000.
- [8] J. Daugman. Probing the uniqueness and randomness of IrisCodes: Results from 200 billion iris pair comparisons. *Proceedings of the IEEE*, vol. 94, no. 11, pag. 1927–1935, 2006.
- [9] J. Daugman. New methods in Iris Recognition. *IEEE Transactions on Systems, Man and Cybernetics - Part B: Cybernetics*, vol. 37, no. 5, pag. 1167–1175, 2007.
- [10] Y. Du, E. Arslanturk, Z. Zhou and C. Belcher. Video-Based Noncooperative Iris Image Segmentation. *IEEE Transactions on Systems, Man and Cybernetics - Part B: Cybernetics*, vol. 41, no. 1, pag. 64–74, 2011.
- [11] R. Duda, P. Hart and D. Stork. Pattern Classification. Wiley-Interscience Publication, ISBN: 978-0-471-05669-0, 2001.
- [12] G. Granlund. Fourier Preprocessing for Hand Print Character Recognition. *IEEE Transactions on Computers*, vol. 21, pag. 195–201, 1972.
- [13] G. Hoffmann. CIE Lab Color Space. <http://docs-hoffmann.de/cielab03022003.pdf>, assessed on June 2013.
- [14] J. Kittler, M. Hatef, R. Duin and J. Matas. On combining classifiers *IEEE Transactions on Pattern Analysis and Machine Intelligence*, vol. 20, no. 3, pag. 226–239, 1998.
- [15] A. Kumar and T-S. Chan. Iris recognition using quaternionic sparse orientation code (QSOC). in Proceedings of the *Computer Vision and Pattern Recognition Workshops*, pag. 59–64, 2012.

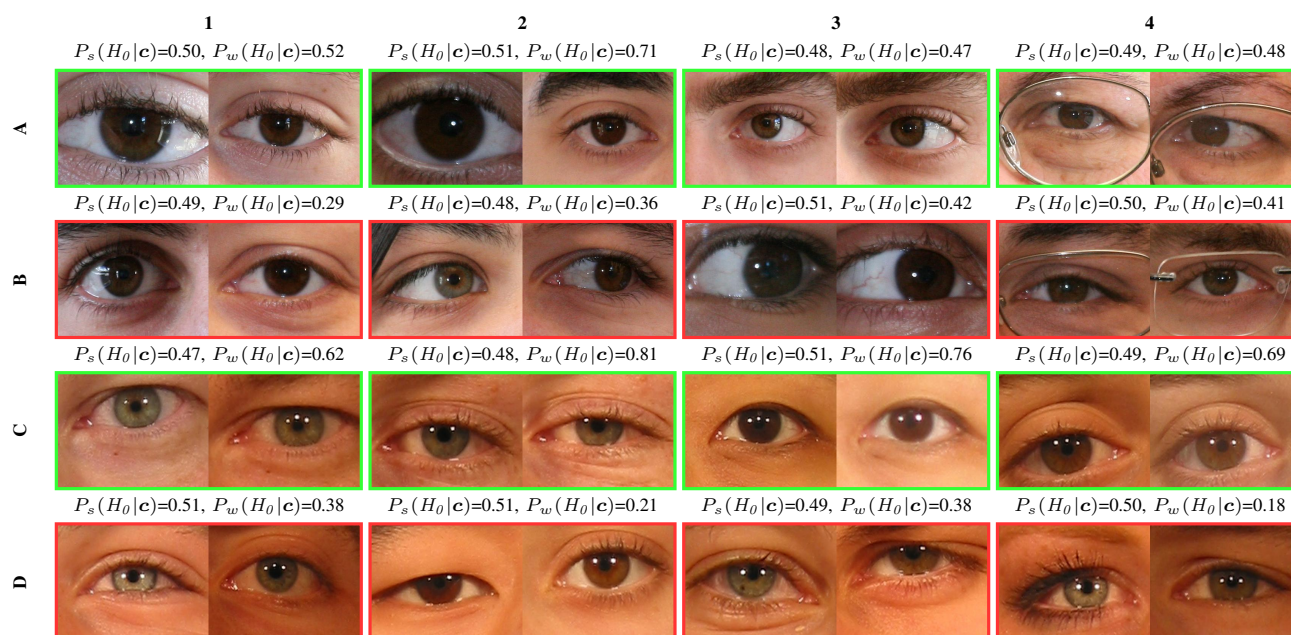


Fig. 14. Examples of image pairwise comparisons that fall in the uncertainty region ( $P_s(H_0|x) \approx 0.5$ ) of the strong biometric expert. In most cases, the weak biometric expert provided valuable information to distinguish between genuine comparisons (green frames) and impostors (red frames). The upper rows (A, B) regard the UBIRIS.v2 dataset and the bottom rows (C, D) are from the FRGC dataset.

[16] A. Kumar, T-S. Chan and C-W. Tan. Human identification from at-a-distance face images using sparse representation of local iris features. in Proceedings of the *International Conference on Biometrics*, pag. 303–309, 2012.

[17] S. Mallat and Z. Zhang. Matching pursuits with time-frequency dictionaries. *IEEE Transactions on Signal processing*, vol. 41, no. 12, pag. 3397–3415, 1993.

[18] P. Meredith and T. Sarna. The physical and chemical properties of eumelanin. *Pigment Cell Research*, vol. 19, pages 572–594, 2006.

[19] K. Oh and K-A. Toh. Extracting sclera features for cancelable identity verification. in Proceedings of the *International Conference on Biometrics*, pag. 245–250, 2012.

[20] K. Oh, B-S. Oh, K-A. Toh, W-Y. Yau and H-L. Eng. Combining sclera and periocular features for multi-modal identity verification. *Neurocomputing*, vol. 128, pag. 185–198, 2014.

[21] T. Ojala, M. Pietikainen and D. Harwood. A Comparative Study of Texture Measures with Classification Based on Feature Distributions. *Pattern Recognition*, vol. 29, pag. 51–59, 1996.

[22] U. Park, R. Jilela, A. Ross and A.K. Jain. Periocular Biometrics in the Visible Spectrum. *IEEE Transactions on Information Forensics and Security*, vol. 6, no. 1, pages 96–106, 2011.

[23] H. Peng, F. Long and C. Ding. Feature selection based on mutual information: criteria of max-dependency, max-relevance, and min-redundancy. *IEEE Transactions on Pattern Analysis and Machine Intelligence*, vol. 27, no. 8, pag. 1226–1238, 2005.

[24] P. J. Phillips, P. J. Flynn, T. Scruggs, K. W. Bowyer, J.Chang, K. Hoffman, J. Marques, J. Min, and W. Worek. Overview of the face recognition grand challenge. In *Proceedings of the IEEE Conference on Computer Vision and Pattern Recognition*, vol. 1, pag. 947–954, 2005.

[25] H. Proença, S. Filipe, R. Santos, J. Oliveira and L. A. Alexandre. The UBIRIS.v2: A Database of Visible Wavelength Iris Images Captured On-The-Move and At-A-Distance. *IEEE Transactions on Pattern Analysis and Machine Intelligence*, vol. 32, no. 8, pag. 1529–1535, 2010.

[26] H. Proença. Iris Recognition: On the Segmentation of Degraded Images Acquired in the Visible Wavelength. *IEEE Transactions on Pattern Analysis and Machine Intelligence*, vol. 32, no. 8, pag. 1502–1516, 2010.

[27] H. Proença and L. A. Alexandre. Toward Covert Iris Biometric Recognition: Experimental Results From the NICE Contests. *IEEE Transactions on Information Forensics and Security*, vol. 7, no. 2, pag. 798–808, 2012.

[28] P. Pudil, J. Ferri, J. Novovičová. Floating search methods for feature selection with nonmonotonic criterion function. Proceedings of the *12<sup>th</sup> International Conference on Pattern Recognition*, vol. 2, 279–283, 1994.

[29] A. Raffei, H. Asmundi, R. Hassan and R. Othman. Feature extraction for different distances of visible reflection iris using multiscale sparse representation of local Radon transform. *Pattern Recognition*, vol. 46, pag. 2622–2633, 2013.

[30] K. Roy, P. Battacharya and C. Suen. Iris recognition using shape-guided approach and game theory. *Pattern Analysis and Applications*, vol. 14, pag. 329–348, 2011.

[31] A. Rahulkar and R. Holambe. Half-Iris Feature Extraction and Recognition Using a New Class of Biorthogonal Triplet Half-Band Filter Bank and Flexible k-out-of-n:A Postclassifier. *IEEE Transactions on Information Forensics and Security*, vol. 7, no. 1, pag. 230–240, 2012.

[32] K. vd Sande, T. Gevers and C. Snoek. Evaluating Color Descriptors for Object and Scene Recognition. *IEEE Transactions on Pattern Analysis and Machine Intelligence*, vol. 32, no. 9, pag. 1582–1596, 2010.

[33] Z. Sun and T. Tan. Ordinal Measures for Iris Recognition. *IEEE Transactions on Pattern Analysis and Machine Intelligence*, vol. 31, no. 12, pages 2211–2226, 2009.

[34] T. Tan, Z. He, and Z. Sun. Efficient and robust segmentation of noisy iris images for non-cooperative iris recognition. *Image and Vision Computing*, vol. 28, no. 2, pag. 223–230, 2010.

[35] C-W. Tan and A. Kumar. Towards Online Iris and Periocular Recognition Under Relaxed Imaging Constraints. *IEEE Transactions on Image Processing*, vol. 22, no. 10, pag. 3751–3765, 2013.

[36] T. Tan, X. Zhang, Z. Sun and H. Zhang. Noisy iris image matching by using multiple cues. *Pattern Recognition Letters*, vol. 33, pag. 970–977, 2012.

[37] P. Trezona. Derivation of the 1964 CIE 10 XYZ Colour-Matching Functions and Their Applicability in Photometry. *Color Research and Application*, vol. 26, no. 1, pag. 67–75, 2001.

[38] Q. Wang, X. Zhang, M. Li, X. Dong, Q. Zhou and Y. Yin. Adaboost and multi-orientation 2D Gabor-based noisy iris recognition. *Pattern Recognition Letters*, vol. 33, pag. 978–983, 2012.

[39] Z. Zhou, E. Du, N. Thomas and E. Delp. A New Human Identification Method: Sclera Recognition. *IEEE Transactions on Systems, Man and Cybernetics - Part A: Systems and Humans*, vol. 42, no. 3, pag. 571–583, 2012.



**Hugo Proença** received the B.Sc. degree from the University of Beira Interior, Portugal, in 2001, the M.Sc. degree from the Faculty of Engineering, University of Oporto, in 2004, and the Ph.D. degree from the University of Beira Interior, in 2007. His research interests are focused in the artificial intelligence, pattern recognition and biometrics. Currently, he serves as Assistant Professor in the Department of Computer Science, University of Beira Interior. He is the area editor (ocular biometrics) of the IEEE Biometrics Compendium Journal and member of the

Editorial Board of the International Journal of Biometrics. Also, he served as Guest Editor of special issues of the Pattern Recognition Letters, Image and Vision Computing and Signal, Image and Video Processing journals.